Energy Reshaping based Passive Fractional-order PID Control Design and Implementation of a Grid-connected PV Inverter for MPPT using Grouped Grey Wolf Optimizer

Bo Yang [1], Tao Yu [2,3,]*, Hongchun Shu [1], Dena Zhu [1], Na An [1], Yiyan Sang [4], Lin Jiang [4]

[1] Faculty of Electric Power Engineering, Kunming University of Science and Technology, 650500 Kunming, China;

[2] College of Electric Power, South China University of Technology, 510640 Guangzhou, China;

[3] Guangdong Key Laboratory of Clean Energy Technology, 510640 Guangzhou, China;

[4] Department of Electrical Engineering & Electronics, University of Liverpool, Liverpool, L69 3GJ, United Kingdom;

* Correspondence: taoyu1@scut.edu.cn, Tel.: +86-130-020-88518

Abstract: This paper designs a novel passive fractional-order proportional-integral-derivative (PFoPID) controller for a grid-connected photovoltaic (PV) inverter via energy reshaping, such that the maximum power point tracking (MPPT) can be achieved through perturb and observe (P&O) technique under different atmospheric conditions. Based on the passivity theory, a storage function associated with the DC-link voltage and DC-link current, as well as q-axis current is firstly constructed for the PV system, in which the physical property (e.g., heat produced on resistors) of each term is thoroughly investigated and analyzed while the beneficial terms are carefully retained in order to fully exploit the essential characteristics of the PV system. Then, the remaining energy of the storage function is reshaped via an additional input in the context of fractional-order PID (FoPID) control framework, which control parameters are optimally tuned by grouped grey wolf optimizer (GGWO), such that an optimal control performance can be realized. Four case studies, including the solar irradiation variation, temperature variation, power grid voltage drop, and PV inverter parameter uncertainties, are carried out. Simulation results verify the effectiveness and advantages of PFoPID control in comparison to that of conventional PID control, fractional-order PID (FoPID) control, and passivity-based control (PBC), respectively. Lastly, a dSpace based hardware-in-loop (HIL) experiment is undertaken to validate the implementation feasibility of the proposed approach.

Keywords: Photovoltaic inverter; MPPT; passivity; fractional-order PID control; energy reshaping

Nomenclature

Variables		N_p	number of panels connected in parallel
V_{dc}	PV output voltage	N_s	number of panels connected in series
I_{pv}	PV output current	V_N	output voltage of the PV array at the Nth sample of time
I_{ph}	cell's photocurrent	R_a, R_b, R_c	line resistance of the grid under abc frame
I_S	cell's reverse saturation current	L_a, L_b, L_c	line inductance of the grid under abc frame
I_{RS}	cell's reverse saturation current at reference solar irradiation and temperature	C	DC bus capacitance
T_c	cell's absolute working temperature, K	Abbreviations	
T_{ref}	cell's reference temperature, K	MPPT	maximum power point tracking
S	total solar irradiation, W/m^2	PV	photovoltaic
E_g	bang-gap energy of the semiconductor used in the cell	FRT	fault ride-through
$I(t)$	output current of the PV array at the tth sample of time	P&O	perturb and observe
$V(t)$	output voltage of the PV array at the (t-1)th sample of time	SVPWM	space vector pulse width modulation
$P(t)$	output current of the PV array at the (t-1)th sample of time	PID	proportional-integral-derivative
$v_{a,b,c}$	three-phase output voltages of the inverter	FoPID	fractional-order PID
$e_{a,b,c}$	three-phase voltages of the grid	PBC	passivity-based control
$i_{a,b,c}$	three-phase currents of the grid	PFoPID	passive fractional-order PID
$v_{d,q}$	d-q components of the output voltage of the inverter	MPP	maximum power point
$e_{d,q}$	d-q components of the grid voltage	AC	alternating current
$i_{d,q}$	d-q components of the grid current	DC	direct current
ω	AC grid synchronous frequency	GGWO	grouped grey wolf optimizer
PV system parameters		The PFoPID control parameters	
q	electron charge, $1.60217733 \times 10^{-19}$ Cb	K_{P1}, K_{P2}	proportional gain
A	p-n junction ideality factor, between 1 and 5	K_{I1}, K_{I2}	integral gain
k	Boltzman's constant, 1.380658×10^{-23} J/K	K_{D1}, K_{D2}	derivative gain
k_i	cell's short-circuit current temperature coefficient	μ_1, μ_2	fractional differentiator order
R_s	cell series resistance	λ_1, λ_2	fractional integrator order

1. Introduction

Among different types of renewable energy resources (RES) (Yang et al., 2016, Liao et al., 2017, Liu et al., 2016, Yang et al., 2018c, 2018d), solar energy technologies are gaining enormous attentions around the globe due to the fact of solar resources abundance, easy installation of solar harvesting technologies, noiseless and safe operation with relatively low operation costs (Kabir et al., 2018). It is economical and crucial for the photovoltaic (PV) systems to always extract the available maximum solar power, such goal can be achieved by regulating the active power and operating the PV system at the unity power factor, which is called the maximum power point tracking (MPPT) (Kandemir et al., 2017). In general, Numerous MPPT techniques have been employed to dynamically adjust the power output of PV systems in the variation of solar irradiation and temperature, such as hill-climbing (Alajmi et al., 2011), perturb & observe (P&O) (Alik and Awang, 2017), and incremental conductance (INC) (Loukriz et al., 2016). After the MPP is obtained, an effective and efficient PV inverter controller is needed to regulate the active power.

Thus far, linear controllers using proportional-integral-derivative (PID) loops are widely adopted for the PV inverter, which own the prominent merits of high operation reliability and structure simplicity (Kadri et al., 2011). However, one essential flaw of PID control is its inconsistent control performance when operation condition varies due to the one-point linearization, such issue becomes quite severe in PV systems as the weather conditions always vary significantly. To handle this thorny obstacle, fractional-order PID (FoPID) control based on fractional calculus has attracted considerable interest in both industry and academics, which basically introduces the fractional integrator and fractional differentiator to enhance the dynamical performance (Malek et al., 2014). In Mitkowski and Oprzedkiewicz (2015), a minimal-energy control of an uncertain-parameter oriented PV system with the use of half-order PID controller was proposed. Moreover, different meta-heuristic optimization techniques were applied to determine the optimal FoPI controller gains of on-gird solar PV systems (Ramadan et al., 2017).

Alternatively, nonlinear controllers provide a powerful tool to remedy the inherent disadvantages of the above linear controllers. Feedback linearization control (FLC) was designed for both the two-level and three-level grid-connected PV inverter in Lalili et al. (2011; 2013), which can fully compensate the PV inverter nonlinearities, such that a global control consistency could be realized in the face of various operation conditions. However, FLC requires an accurate PV system model thus it is very sensitive to parameter uncertainties or external disturbances. Naghmasha et al., (2018) designed a backstepping MPPT controller for PV systems under various solar irradiation and temperature levels, whose asymptotic stability is guaranteed through Lyapunov stability analysis. Moreover, adaptive multi-context cooperatively coevolving particle swarm optimization (AMCCPSO) was employed to solve the MPPT of large-scale PV arrays on the green ocean-going ship model offline, in which the model predictive control (MPC) was adopted to achieve the online MPPT control in real-time (Tang et al., 2017). In Kchaou et al., (2017), a robust MPPT technique based on the second-order sliding mode control (SMC) strategy was presented, which overcomes the chattering phenomenon of the classical first-order SMC and ensures a higher accuracy even with system imperfections. Besides, a backstepping finite time fast sliding mode (BFTSM) control was proposed to offer invariant stability to modelling uncertainties due to the inverter parameter changes, variations in system frequency and exogenous inputs (Dhar and Dash, 2016). Based on the pole placement method, a disturbance estimator was adopted for the digital predictive current controller so as to minimize its sensitivity to parameter uncertainties and to efficiently reject the grid-side disturbances (Mohomad et al., 2017).

However, the aforementioned approaches merely regard the PV systems control as a pure mathematical problem while their physical characteristics are ignored or not thoroughly examined. In fact, these physical properties usually play an important role for the dynamical responses of a physical system. Hence, passivity-based control (PBC) offers an invaluable insight of physical features of engineering problems. More specifically, it treats a dynamical system as an virtual energy-transformation device, which can flexibly decompose a complex original system into several simpler subsystems via proper interconnection and adding up their local/distributed energies to determine the overall systems behaviour described by a storage function (Ortega et al., 2001). Further, the action of a controller connected to the dynamical system may also be viewed, in terms of energy, as another separate dynamical system. Therefore, the control problem could be considered as seeking an appropriate interconnection pattern between the controller and the dynamical system, such that the real-time variations of the storage function could take a desired form (Ortega et al., 2008). As a consequence, PBC is promising to achieve a satisfactory control performance for the PV system as it is essentially a typical energy-transformation device, e.g., transform the solar energy into the electricity. A passivity-based MPPT controller was presented in Bao et al., (2012) for grid-connected PV system, which ensures a rapid and accurate PV system response to the changes of external environment conditions. In addition, PBC was synthesized via the energy shaping and damping injection techniques for power management of PV/battery hybrid power source (Tofighi and Kalantar, 2011). In Mojallizadeh and Badamchizadeh (2016), an adaptive passivity-based controller (APBC) was developed for PV/battery hybrid power source via an algebraic parameter identifier, which can estimate the unknown parameters

2

of PV array voltage, battery voltage, and load resistance. Other applications of PBC include permanent magnetic synchronous generator (PMSG) (Yang et al., 2018a) or doubly-fed induction generator (DFIG) (Song and Qu, 2013) based wind energy conversion systems, fuel cell systems (Hilairet et al., 2015), battery energy storage systems (Kanchanaharuthai et al., 2015), etc.

In general, linear control has the advantages of high reliability and structure simplicity but disadvantages of control performance inconsistency; meanwhile, nonlinear control owns the strength of improved control performance but weakness of high complexity. Based on the above discussions, this paper aims to design a novel hybrid framework of FoPID control and PBC, such that their merits could be collaboratively exploited while their demerits could also be largely reduced, which is called passive fractional-order PID (PFoPID) control, with the following three design stages:

● *Beneficial terms retainment*: A storage function associated with the DC-link voltage and DC-link current, as well as q-axis current is constructed for the PV system, in which the physical property of each term is thoroughly investigated and analyzed while the beneficial terms are carefully retained to fully exploit the essential characteristics of the PV system;

● *Energy reshaping*: An additional input is introduced with the FoPID control framework to reshape the retained energy of the storage function, such that an enhanced control performance can be realized.

● *Parameter optimizing*: The newly proposed meta-heuristic algorithm called grouped grey wolf optimizer (GGWO) (Yang et al., 2017) is employed to seek the optimal PFoPID control parameters.

The advantages of this paper to the existing work are summarized as:

(1) Compared to the linear FoPID control (Mitkowski and Oprzedkiewicz, 2015; Ramadan, 2017), which control performance might be degraded when operation condition varies due to the one-point linearization. In contrast, PFoPID is a nonlinear method which removes all the detrimental nonlinearities thus can achieve a globally consistent control performance under various operation points;

(2) Compared to FLC (Lalili et al., 2011; 2013) which fully removes all nonlinearities, PFoPID control retains the beneficial nonlinearities by carefully examining the physical property of the PV system, such that an improved control performance with clear physical interpretation can be achieved;

(3) Compared to other typical meta-heuristic algorithms such as genetic algorithm (GA) (Messai et al., 2011), particle swarm optimization (PSO) (Ishaque et al., 2012), artificial bee colony (ABC) (Oshaba et al., 2016), cuckoo search (CS) (Ahmed and Salam, 2014), teaching-learning-based optimization (TLBO) (Rezk and Fathy, 2107). This paper adopts GGWO which modifies the wolf hunting hierarchy by introducing additional wolf roles to realize a proper trade-off between exploration and exploitation, such that a better optimization of control parameters can be realized.

Besides, this paper is a novel interdisciplinary work which contribution/novelty to the field of solar energy is given as follows:

(a) *Satisfactory MPPT and current regulation*: PFoPID control can significantly accelerate the tracking performance of DC-link voltage and rapidly regulate the q-axis current without overshoot. Thus, a more stable power output and rapid current regulation could be obtained, such that a higher power production is achieved under various atmospheric conditions;

(b) *Economical operation*: PFoPID control just requires the minimum control costs of PV inverter. Thus, PV system can operate more economically with significant energy saving during the whole operation life of PV systems;

(c) *Practical application*: A dSpace based hardware-in-loop (HIL) experiment is carried out which validates the implementation feasibility of the proposed approach. Hence, PFoPID control is promising to be applied on PV inverters in practice.

The rest of this paper is organized as follows: Section 2 attempts to model the grid-connected PV inverter. In Section 3, some preliminaries of PBC and FoPID control are recalled. Moreover, PFoPID control is applied on PV inverter for MPPT in Section 4. Then, case studies are carried out in Section 5. In section 6, a dSpace based HIL experiment is presented. At last, Section 7 concludes the whole paper.

2. Modelling of Grid-connected PV Inverter

The configuration of a single-stage grid-connected PV inverter is demonstrated in Fig. 1, which consists of a PV array, a DC-link capacitor, a three-phase two-level inverter, and a three-phase power grid (Kadri, et al., 2011).
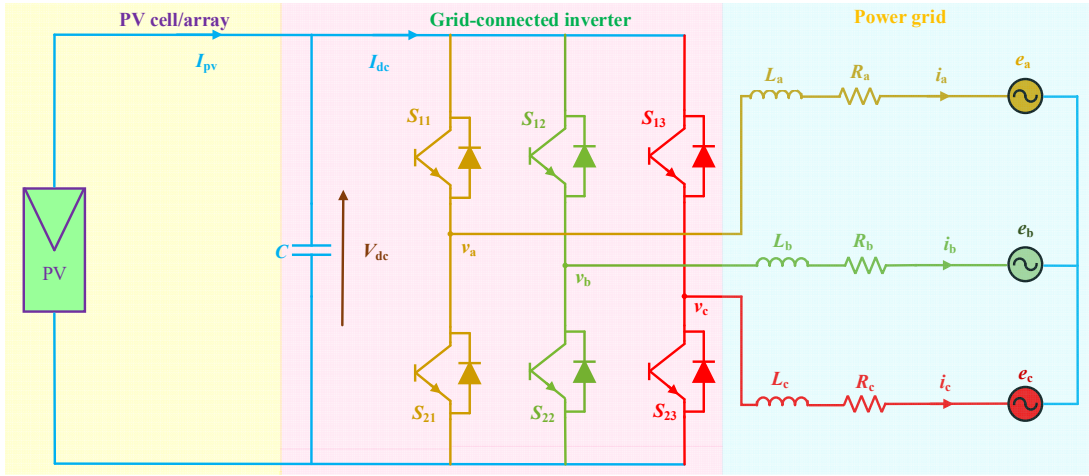
Figure 1. The configuration of a three-phase two-level grid-connected PV inverter.

Denote the number of PV cells in series and in parallel to be N_s and N_p, respectively, the relationship between the output current and voltage can be described by (Lalili et al., 2011; 2013)

$$I_{pv} = N_p I_{ph} - N_p I_s \left(\exp\left[\frac{q}{AKT_c} \left(\frac{V_{dc}}{N_s} + \frac{R_s I_{pv}}{N_p} \right) \right] - 1 \right) \tag{1}$$

where the meaning of each symbol is given in Nomenclature.

The generated photocurrent I_{ph} is determined by the solar irradiation, as follows

$$I_{ph} = \left(I_{sc} + k_i (T_c - T_{ref}) \right) \frac{S}{1000} \tag{2}$$

Moreover, the PV cell's saturation current I_s changes with the temperature based on the following relationship:

$$I_s = I_{RS} \left[\frac{T_c}{T_{ref}} \right]^3 \exp\left[\frac{q E_g}{Ak} \left(\frac{1}{T_{ref}} - \frac{1}{T_c} \right) \right] \tag{3}$$

Here, a PV array of 30 panels in series is employed while each module contains 36 cells in series (Lalili et al., 2011), respectively.

The dynamics of the three-phase two-level PV inverter in dq frame can be described as (Lalili et al., 2011)

$$\begin{cases} v_d = e_d + R i_d + L \frac{di_d}{dt} + \omega L i_q \\ v_q = e_q + R i_q + L \frac{di_q}{dt} - \omega L i_d \end{cases} \tag{4}$$

where e_d, e_q, i_d, i_q, v_d, and v_q denote the dq-axis components of grid voltage, grid current, and PV inverter output voltage, respectively; R and L represent the equivalent resistance and inductance, respectively; while ω denotes the AC grid synchronous frequency. Ignore the power losses in PV inverter switches, the power balance relationship between the DC input side and the AC output side can be described as

$$e_d i_d + e_q i_q = V_{dc} I_{dc} \tag{5}$$

where V_{dc} and I_{dc} are the input voltage and current of the PV inverter, respectively.

The dynamics of the DC side is obtained by applying Kirchhoff's current law, as follows

$$C \frac{dV_{dc}}{dt} = I_{pv} - I_{dc} = I_{pv} - \frac{e_d i_d + e_q i_q}{V_{dc}} \tag{6}$$

where C is the DC bus capacitance.

This paper merely considers the uniform solar irradiation condition, e.g., there exists no partial shading effect. Hence, the *P-V* curve of PV module has only one peak. Here, P&O technique (Alik and Awang, 2017) is adopted to efficiently track the maximum power point (MPP) under fast time-varying atmospheric conditions.

3 Preliminaries

3.1 Passivity-based control and energy reshaping

The goal of PBC is to passivize a given system with a storage function (a function describing the system energy) which has a minimum at the desired equilibrium point. In the design procedure, PBC attempts to reshape the system energy and to assign a closed-loop energy function equals to the difference between the energy of the system and the energy supplied by the controller.

The energy balancing equation can be written as follows (Ortega et al., 2001):

$$\underbrace{H[x(t)] - H[x(0)]}_{\text{stored}} = \underbrace{\int_0^t u^T(s) y(s) ds}_{\text{supplied}} - \underbrace{d(t)}_{\text{dissipated}} \tag{7}$$

where $H(x)$ is the storage function, and $d(t)$ is a nonnegative function that characterizes the dissipation effects in

4

practical engineering problems, such as friction and heat. Undoubtedly, energy balancing is a universal property of physical systems, which captures a very broad range of applications that include nonlinear and time-varying dynamics (Ortega et al., 2001, 2008).

3.2 Fractional-order PID control

Fractional-order calculus is a generalization of integration and differentiation to non-integer order form, the fundamental operator $_aD_t^\alpha$ is defined as (Podlubny, 1999)

$$_aD_t^\alpha = \begin{cases} \frac{d^\alpha}{dt^\alpha}, & \alpha > 0 \\ 1, & \alpha = 0 \\ \int_a^t (d\tau)^{-\alpha}, & \alpha < 0 \end{cases} \tag{8}$$

where a and t are the lower and upper limits while $\alpha \in \mathcal{R}$ is the operation order.

Here, Riemann-Liouville (RL) definition for fractional-order derivative is adopted with *Gamma* function $\Gamma(\cdot)$, as follows

$$_aD_t^\alpha f(t) = \frac{1}{\Gamma(n-\alpha)} \frac{d^n}{dt^n} \int_a^t \frac{f(\tau)}{(t-\tau)^{\alpha-n+1}} d\tau \tag{9}$$

where n is the first integer which is not less than α, e.g., $n-1 \le \alpha < n$.

Moreover, the RL definition for fractional-order integral is used as

$$_aD_t^{-\alpha} f(t) = \frac{1}{\Gamma(\alpha)} \int_a^t (t-\tau)^{\alpha-1} f(\tau) d\tau \tag{10}$$

with

The Laplace transformation of the RL fractional-order derivative (9) can be obtained as

$$\int_0^\infty {}_0D_t^\alpha f(t) e^{-st} dt = s^\alpha \mathcal{L}\{f(t)\} - \sum_{k=0}^{n-1} s^k {}_0D_t^{\alpha-k-1} f(t)|_{t=0} \tag{11}$$

where $\mathcal{L}\{\cdot\}$ represents the Laplace operator. Under the zero initial conditions, the fractional-order integration with the operation order α can be represented by the transfer function $F(s) = 1/s^\alpha$ in the frequency domain.

The transfer function of FoPID control is given by

$$G(s) = K_P + \frac{K_I}{s^\lambda} + K_D s^\mu \tag{12}$$

where K_P, K_I and K_D are the proportional gain, integral gain, and derivative gain, respectively. In addition, λ and μ (between 0 to 2) denote the fractional integrator order and fractional differentiator order, respectively. The introduction of these two additional parameters can significantly tune the dynamics of many physical systems.

3.3 Grouped grey wolf optimizer

GGWO introduces a grouping mechanism to achieve a wider and deeper collaboration among a specific tribe of grey wolves, which can significantly enhance the global optimum searching performance and can provide an efficient and effective tool for controller parameter tuning in various engineering problems (Yang et al., 2017).

The prey encircling strategy is given as follows:

$$\vec{D} = \left| \vec{C} \cdot \overrightarrow{X_p}(t) - \vec{X}(t) \right| \tag{13}$$

$$\vec{X}(t+1) = \overrightarrow{X_p}(t) - \vec{A} \cdot \vec{D} \tag{14}$$

$$\vec{A} = 2\vec{\alpha} \cdot \vec{r_1} - \vec{\alpha} \tag{15}$$

$$\vec{C} = 2 \cdot \vec{r_2} \tag{16}$$

where t denotes the current iteration; $\vec{X}_p$ and $\vec{X}$ are the location vectors of a prey and a grey wolf, respectively; $\vec{A}$ and $\vec{C}$ are the coefficient vectors, $\vec{\alpha}$ is the encircling coefficient vector, which components are linearly decreased from 2 to 0 during each iteration; while $\vec{r_1}$ and $\vec{r_2}$ are the random vectors uniformly spanned in [0, 1], respectively.

The hunting group strategy is described by

$$\begin{cases} \vec{D}_\alpha = \left| \vec{C}_1 \cdot \vec{X}_\alpha - \vec{X} \right|, \vec{D}_{\beta1} = \left| \vec{C}_2 \cdot \vec{X}_{\beta1} - \vec{X} \right|, \vec{D}_{\beta2} = \left| \vec{C}_2 \cdot \vec{X}_{\beta2} - \vec{X} \right| \\ \vec{D}_{\delta1} = \left| \vec{C}_3 \cdot \vec{X}_{\delta1} - \vec{X} \right|, \vec{D}_{\delta2} = \left| \vec{C}_3 \cdot \vec{X}_{\delta2} - \vec{X} \right|, \vec{D}_{\delta3} = \left| \vec{C}_3 \cdot \vec{X}_{\delta3} - \vec{X} \right| \end{cases} \tag{17}$$

$$\begin{cases} \vec{X}_1 = \vec{X}_\alpha - \vec{A}_1 \cdot \left(\vec{D}_\alpha \right), \vec{X}_{21} = \vec{X}_{\beta1} - \vec{A}_2 \cdot \left(\vec{D}_{\beta1} \right), \vec{X}_{22} = \vec{X}_{\beta2} - \vec{A}_2 \cdot \left(\vec{D}_{\beta2} \right) \\ \vec{X}_{31} = \vec{X}_{\delta1} - \vec{A}_3 \cdot \left(\vec{D}_{\delta1} \right), \vec{X}_{32} = \vec{X}_{\delta2} - \vec{A}_3 \cdot \left(\vec{D}_{\delta2} \right), \vec{X}_{33} = \vec{X}_{\delta3} - \vec{A}_3 \cdot \left(\vec{D}_{\delta3} \right) \end{cases} \tag{18}$$

$$\begin{cases} \vec{X}(t+1) = k_\alpha \vec{X}_1 + k_\beta \left(\frac{\vec{X}_{21} + \vec{X}_{22}}{2} \right) + k_\delta \left(\frac{\vec{X}_{31} + \vec{X}_{32} + \vec{X}_{33}}{3} \right) \\ k_\alpha + k_\beta + k_\delta = 1, k_\alpha \ge 0, k_\beta \ge 0, k_\delta \ge 0 \end{cases} \tag{19}$$

where $\vec{X}_\alpha$, $\vec{X}_\beta$, and $\vec{X}_\delta$ are the locations of α, β, and δ_1 wolves, respectively; while k_α, k_β, and k_δ are the guiding coefficients of α, β, and δ_1 wolves, respectively.

The random scout strategy is given by

$$\vec{X}(t+1) = \vec{X}(t) + \vec{r}_{\delta 2} \tag{20}$$

where $\vec{r}_{\delta 2}$ is a random scout vector which range is arbitrary and merely limited by the upper and lower bound of the controllable variables.

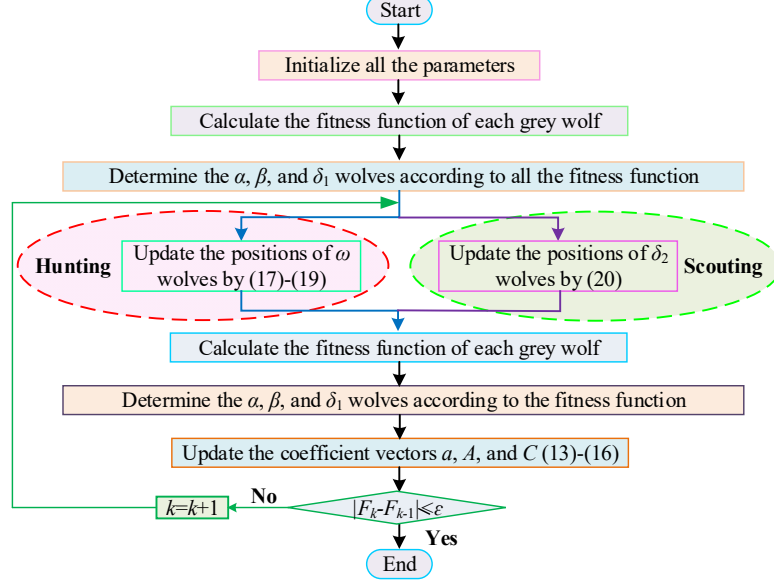The optimization flowchart of GGWO is summarized in Fig. 2.

Figure 2. Optimization flowchart of GGWO.

where ε is the tolerance of convergence error, which value is chosen to be 10^{-4} in this paper; F_k and F_{k-1} represent the fitness function value calculated at the kth iteration and (k-1)th iteration, respectively.

Note that GGWO can effectively avoid the local optimum by the following mechanism: The grey wolves are divided into two independent groups, including a cooperative hunting group and a random scout group. The former one contains four types of grey wolves (i.e., alpha, beta, delta, and omega) to accomplish an effective hunting based on their hierarchical cooperation and three elaborative manoeuvres in the presence of an unknown environment, e.g., prey searching, prey encircling, and prey attacking, of which the number of beta and delta wolves is increased to achieve a deeper exploitation. On the other hand, the latter one undertakes a randomly global search and realizes an appropriate trade-off between the exploration and exploitation. The global optimum seeking performance of GGWO compared to other typical meta-heuristic algorithms can be found in (Yang et al., 2017).

4 PFoPID Control Design of PV Inverter for MPPT using GGWO

4.1 Controller design

P&O technique (Alik and Awang, 2017) for MPPT under various atmospheric conditions is used to obtain the reference of DC-link voltage V_{dc}^*. Meanwhile, the reference of q-axis current i_q^* is determined by the PV inverter operator/utilizer to regulate the power factor, usually it is regulated to maintain a unity power factor.

Define the state vector as $x = (x_1, x_2, x_3)^T = (i_d, i_q, V_{dc})^T$, output $y = (y_1, y_2)^T = (i_q, V_{dc})^T$, and input $u = (u_1, u_2)^T = (v_d, v_q)^T$. The state equation of PV inverter (4) and (6) can be written as

$$\dot{x} = \begin{pmatrix} -\frac{R}{L}x_1 - \omega x_2 - \frac{e_d}{L} \\ -\frac{R}{L}x_2 + \omega x_1 - \frac{e_q}{L} \\ \frac{I_{pv}}{C} - \frac{e_d x_1 + e_q x_2}{C x_3} \end{pmatrix} + \begin{pmatrix} \frac{1}{L} & 0 \\ 0 & \frac{1}{L} \\ 0 & 0 \end{pmatrix} u \tag{21}$$

Define the tracking error $e=[e_1, e_2]^T=[i_q-i_q^*, V_{dc}-V_{dc}^*]^T$. Differentiate the tracking error e until the control input u appears explicitly, yields

$$\begin{bmatrix} \dot{e}_1 \\ \ddot{e}_2 \end{bmatrix} = \begin{bmatrix} f_1(x) \\ f_2(x) \end{bmatrix} + B(x) \begin{bmatrix} u_1 \\ u_2 \end{bmatrix} - \begin{bmatrix} \dot{i}_q^* \\ \ddot{V}_{dc}^* \end{bmatrix} \tag{22}$$

where

$$f_1(x) = -\frac{R}{L}i_q + \omega i_d - \frac{e_q}{L} \tag{23}$$

$$f_2(x) = \frac{I_{pv}}{C} - \frac{e_d\left(-\frac{R}{L}i_d - \omega i_q - \frac{e_d}{L}\right) + e_q\left(-\frac{R}{L}i_q + \omega i_d - \frac{e_q}{L}\right)}{C V_{dc}} - \frac{(e_d i_d + e_q i_q)}{C^2 V_{dc}^2} I_{pv} + \frac{(e_d i_d + e_q i_q)^2}{C^2 V_{dc}^3} \tag{24}$$

with $B(x) = \begin{bmatrix} 0 & \frac{1}{L} \\ -\frac{e_d}{LCV_{dc}} & -\frac{e_q}{LCV_{dc}} \end{bmatrix}$. In order to ensure the above input-output linearization to be valid, the control gain matrix $B(x)$ must be nonsingular among the whole operation range, which requires

$$\det[B(x)] = \frac{e_d}{L^2 CV_{dc}} \neq 0 \tag{25}$$

As component e_d is always different from zero, the above condition can always be satisfied.

A candidate storage function for system (22) can be constructed as

$$H(i_q, V_{dc}, I_{dc}) = \underbrace{\frac{1}{2}\left(i_q - i_q^*\right)^2}_{\text{AC series}-\text{resistor heat}} + \underbrace{\frac{1}{2}(V_{dc} - V_{dc}^*)^2}_{\text{DC parallel}-\text{resistor heat}} + \underbrace{\frac{1}{2}\left(\frac{I_{dc}}{C} - \dot{V}_{dc}^*\right)^2}_{\text{DC series}-\text{resistor heat}} \tag{26}$$

Here, the storage function $H(i_q, V_{dc}, I_{dc})$ can be interpreted as the sum of the heat produced by q-axis current i_q flowing through a virtual unit AC series-resistor, the heat produced by DC-link voltage V_{dc} across a virtual unit DC parallel-resistor, and the heat generated by DC-link current I_{dc} flowing through a virtual unit DC series-resistor associated with DC-link capacitor, respectively.

Remark 1. The first term of the storage function, e.g., $\frac{1}{2}\left(i_q - i_q^*\right)^2$, describes the regulation of power factor; Meanwhile, the latter two terms of the storage function, e.g., $\frac{1}{2}(V_{dc} - V_{dc}^*)^2$ and $\frac{1}{2}\left(\frac{I_{dc}}{C} - \dot{V}_{dc}^*\right)^2$, illustrate the energy-transformation process from the solar energy into the electricity. The variation of PV output power I_{pv} can be directly reflected by the change of DC-link voltage V_{dc} and DC-link current I_{dc} based on DC-link relationship (6).

Differentiate storage function $H(i_q, V_{dc}, I_{dc})$ with respect to the time, yields

$$\dot{H}(i_q, V_{dc}, I_{dc}) = \left(i_q - i_q^*\right)\left(-\frac{R}{L}i_q + \omega i_d - \frac{e_q}{L} + \frac{1}{L}u_2 - \dot{i}_q^*\right) + \left(\frac{I_{dc}}{C} - \dot{V}_{dc}^*\right)$$
$$\left[V_{dc} - V_{dc}^* + \frac{i_{pv}}{C} - \frac{e_d\left(-\frac{R}{L}i_d - \omega i_q - \frac{e_d}{L}\right) + e_q\left(-\frac{R}{L}i_q + \omega i_d - \frac{e_q}{L}\right)}{CV_{dc}} - \frac{(e_d i_d + e_q i_q)}{C^2 V_{dc}^2}I_{pv} \right. \tag{27}$$
$$\left. + \frac{(e_d i_d + e_q i_q)^2}{C^2 V_{dc}^3} - \frac{e_d}{LCV_{dc}}u_1 - \frac{e_q}{LCV_{dc}}u_2 + \ddot{V}_{dc}^*\right]$$

Design PFoPID control for system (22) as

$$\begin{cases} u_1 = -\frac{LCV_{dc}}{e_d}\left[\ddot{V}_{dc}^* - V_{dc} + V_{dc}^* + \frac{e_q}{LCV_{dc}}u_2 - \frac{i_{pv}}{C} + \frac{e_d\left(-\frac{R}{L}i_d - \omega i_q - \frac{e_d}{L}\right) + e_q\left(-\frac{R}{L}i_q + \omega i_d - \frac{e_q}{L}\right)}{CV_{dc}} + \frac{(e_d i_d + e_q i_q)}{CV_{dc}^2}\dot{V}_{dc}^* - v_1\right] \\ u_2 = Li_q^* - \omega L i_d + R i_q^* + e_q - v_2 \end{cases} \tag{28}$$

with the additional inputs v_1 and v_2 being designed in the FoPID control form, as follows

$$\begin{cases} v_1 = K_{P1}(V_{dc} - V_{dc}^*) + \frac{K_{I1}}{s^{\lambda_1}}(V_{dc} - V_{dc}^*) + K_{D1}s^{\mu_1}(V_{dc} - V_{dc}^*) \\ v_2 = K_{P2}\left(i_q - i_q^*\right) + \frac{K_{I2}}{s^{\lambda_2}}\left(i_q - i_q^*\right) + K_{D2}s^{\mu_2}\left(i_q - i_q^*\right) \end{cases} \tag{29}$$

where PID control gains $K_{P1}, K_{P2}, K_{I1}, K_{I2}, K_{D1}, K_{D2}$, fractional differentiator order μ_1 and μ_2, fractional integrator order λ_1 and λ_2, are chosen to ensure a satisfactory convergence of tracking error dynamics (22).

Substitute PFoPID control (28) and (29) into the derivative of the storage function (27), together with the DC-link relationship (6), yields

$$\dot{H}(i_q, V_{dc}, I_{dc}) = \underbrace{-\frac{1}{CR_{dc}}\left(\dot{V}_{dc} - \dot{V}_{dc}^*\right)^2 - \frac{R}{L}\left(i_q - i_q^*\right)^2}_{\text{beneficial terms retainment}} - \underbrace{\left(\dot{V}_{dc} - \dot{V}_{dc}^*\right)v_1 - \frac{i_q - i_q^*}{L}v_2}_{\text{energy reshaping}} \tag{30}$$

where $R_{dc} = \frac{V_{dc}^2}{e_d i_d + e_q i_q}$ represents a virtual resistor in parallel with DC-link capacitor.

Here, the first two terms of system (30) are carefully retained as they are beneficial terms of the PV system, which can accelerate the tracking rate of q-axis current i_q and DC-link voltage V_{dc}. Meanwhile, the last two terms of system (30) are incorporated with FoPID control framework, which guarantees that such energy could be desirably dissipated through carefully tuning the FoPID control parameters to further accelerate the decrease rate of the storage function, i.e., an improved dynamics of the closed-loop system can be realized.

Remark 2. It is worth noting that tracking error dynamics (22) is transformed into an equivalent linear system by the PFoPID control, e.g., all the detrimental terms have been fully removed (both in the linear and nonlinear form) while the beneficial terms (only in the linear form) are retained. Hence, its control parameters could be chosen based on this equivalent linear system, such that a globally control consistency could be realized. Therefore, it can simultaneously own the merits of high reliability of linear controllers and the merits of globally consistent control

performance of nonlinear controllers. Lastly, as the beneficial terms are remained, PFoPID control can outperform the FLC, which removes all terms without any consideration of the property of each terms.

Remark 3. The conventional linear PID control scheme employs an inner current loop to regulate the inverter current (Kadri et al., 2011), such that the closed-loop PV system stability could be guaranteed during severe faults as the magnitude of inner currents are bounded in the safe operation range (normally set by the manufacturer). In contrast, the proposed PFoPID control (28)-(29) is a nonlinear control scheme which is derived from passivity theory, it actually contains no inverter current in its control law thus no inverter current loop and no inverter current measurement/feedback is used. In order to ensure the stability of the closed-loop PV system by PFoPID control, an additional overcurrent protection device (Zhao et al., 2011; Abdel-Salam et al., 2015) are employed which will be activated to prevent the overcurrent of PV systems (Yang et al., 2018b).

4.2 Optimal control parameter tuning

The PFoPID control parameters in Eq. (29) are optimally tuned through GGWO under three cases, e.g., (a) Solar irradiation variation, (b) Temperature variation, and (c) Power grid voltage drop. The optimization goal is to minimize the tracking error of DC-link voltage and q-axis current, together with the minimization of the overall control costs, which model is given as follows

$$\text{Minimize } F(\mathbf{x}) = \sum\nolimits_{\text{Three cases}} \int_0^T \left(|V_{dc} - V_{dc}^*| + \left|i_q - i_q^*\right| + \omega_1|u_1| + \omega_2|u_2| \right) dt$$

$$\text{subject to } \begin{cases} K_{Pi}^{\min} \le K_{Pi} \le K_{Pi}^{\max} \\ K_{Ii}^{\min} \le K_{Ii} \le K_{Ii}^{\max} \\ K_{Di}^{\min} \le K_{Di} \le K_{Di}^{\max} \\ \lambda_i^{\min} \le \lambda_i \le \lambda_i^{\max} \\ \mu_i^{\min} \le \mu_i \le \mu_i^{\max} \\ u_i^{\min} \le u_i \le u_i^{\max} \end{cases}, \quad i=1,2. \tag{31}$$

where the weights ω_1 and ω_2 are used to scale the magnitude of control costs which are chosen to be 1/5. T=3 s denotes the simulation time and the control costs are bounded by their limits.

The proportional gains K_{Pi} lie in [0, 300], integral gains K_{Ii} are between [0, 200], derivative gains K_{Di} are among [0, 50], fractional integrator orders μ_i and differentiator orders λ_i are bounded in [0, 2], respectively. As the control inputs may exceed the admissible capacity of the PV inverter at some operation points, their values are bounded in [-0.6, 0.6] per unit (p.u.). The GGWO parameters are chosen as guiding coefficients of α wolf k_α=0.3, β wolf k_β=0.4, δ_1 wolf k_δ=0.3, the population size of the cooperative hunting group n_h=12, and the population size of the random scout group n_s=6, respectively (Yang et al., 2017).

The global optimum search ability of GGWO can be enhanced compared with that of GWO (Mirjalili et al., 2014) due to its wider exploration and deep exploitation, as follows:

- The original GWO employs four types of wolves for cooperative hunting, in which the ω wolves are guided by the other three wolves, i.e., α, β, and δ wolves with the best solution. Hence, GWO may be easily trapped at a local optimum as the searching direction is generally concentrated to merely three wolves. In contrast, the number of β and δ wolves in GGWO for cooperative hunting is increased to two and three, respectively, which can lead to a wider searching direction for ω wolves (six wolves instead of three wolves). Therefore, the cooperative hunting group of GGWO can effectively avoid a local optimum.

- Compared with GWO, GGWO introduces a novel random scout group to randomly search for a potential prey in the unknown environment, whose searching strategy is completely independent from others. Under such framework, the probability of obtaining a high-quality optimum with a smaller fitness function can be increased, thus a local optimum can be effectively avoided by the introduction of random scout group.

The PFoPID control performance is evaluated and compared to that of PID control (Kadri et al., 2011), FoPID control (Malek et al., 2014), and PBC (Bao et al., 2012), respectively. In order to achieve a fair comparison, the parameters of these four controllers are all optimally tuned by GGWO. GGWO runs for 30 times and the best results (the control parameters resulting in the lowest fitness function) are adopted for each controller. The obtained results can be found in Table 1 while the statistic results are tabulated in Table 2, respectively. From Table 2, it can be seen that PBC requires the least convergence time as it has only two parameters that need to be tuned. Moreover, FoPID control can obtain a lower fitness function than that of PID control due to the improvement by fractional-order mechanism. At last, PFoPID control owns the lowest fitness function thus it has the best control performance among all controllers.

Table 1
The optimal control parameters of different controllers obtained by GGW in 30 runs.

Algorithm	q-axis current			DC-link voltage		
PID	$K_{P1} = 197$	$K_{I1} = 126$	$K_{D1} = 55$	$K_{P2} = 173$	$K_{I2} = 116$	$K_{D2} = 73$
FoPID	$K_{P1} = 185$	$K_{I1} = 147$	$K_{D1} = 25$	$K_{P2} = 148$	$K_{I2} = 182$	$K_{D2} = 51$
	$\mu_1 = 1.63$	$\lambda_1 = 1.25$		$\mu_2 = 1.44$	$\lambda_2 = 1.93$	
PBC	$\lambda_1 = 35$			$\lambda_2 = 57$		
PFoPID	$K_{P1} = 120$	$K_{I1} = 85$	$K_{D1} = 10$	$K_{P2} = 165$	$K_{I2} = 120$	$K_{D2} = 15$
	$\mu_1 = 1.75$	$\lambda_1 = 1.5$		$\mu_2 = 1.5$	$\lambda_2 = 1.25$	

Table 2

The statistical results of obtained by different controllers in 30 runs.

Algorithm	Fitness function (p.u.)			Convergence time (hour)			Iteration number of convergence		
	Max.	Min.	Mean	Max.	Min.	Mean	Max.	Min.	Mean
PID	2.18	1.64	1.89	0.51	0.42	0.47	176	153	162
FoPID	1.87	1.48	1.55	0.45	0.33	0.38	145	113	136
PBC	1.34	1.07	1.22	0.14	0.11	0.13	52	24	33
PFoPID	1.17	0.92	1.03	0.64	0.51	0.57	164	141	153

4.3 Controller bandwidth

The closed-loop system of the PV inverter is given as

$$\begin{cases} \dot{e}_1 + (K_{P2} + \frac{R}{L})e_1 + \frac{K_{I2}}{s^{\lambda_2}}e_1 + K_{D2}s^{\mu_2}e_1 = 0 \\ \ddot{e}_2 + \frac{1}{CR_{dc}}\dot{e}_2 + K_{P1}e_2 + \frac{K_{I1}}{s^{\lambda_1}}e_2 + K_{D1}s^{\mu_1}e_2 = 0 \end{cases} \tag{32}$$

One can obtain the transfer function of the closed-loop system (32) as

$$\begin{cases} \phi_1(s) = \dfrac{1}{1 + \dfrac{s + \frac{R}{L}}{K_{D2}s^{\mu_2} + \frac{K_{I2}}{s^{\lambda_2}} + K_{P2}}} \\ \phi_2(s) = \dfrac{1}{1 + \dfrac{CR_{dc}s^2 + 1}{CR_{dc}(K_{D1}s^{\mu_1} + \frac{K_{I1}}{s^{\lambda_1}} + K_{P1})}} \end{cases} \tag{33}$$

The bandwidth of the PFoPID controller is calculated as

$$\begin{cases} |\phi_1(j\omega_{b1})| = \frac{1}{\sqrt{2}} \Rightarrow \left| 1 + \dfrac{j\omega_{b1} + \frac{R}{L}}{K_{D2}(j\omega_{b1})^{\mu_2} + \frac{K_{I2}}{(j\omega_{b1})^{\lambda_2}} + K_{P2}} \right| = \sqrt{2} \\ |\phi_2(j\omega_{b2})| = \frac{1}{\sqrt{2}} \Rightarrow \left| 1 + \dfrac{-CR_{dc}\omega_{b2}^2 + 1}{CR_{dc}(K_{D1}(j\omega_{b2})^{\mu_1} + \frac{K_{I1}}{(j\omega_{b2})^{\lambda_1}} + K_{P1})} \right| = \sqrt{2} \end{cases} \tag{34}$$

Note that the explicit solution of equation (34) is extremely difficult, if not impossible, to obtain due to the fractional-order differentiator and integrator. To handle this issue, the solution scanning method is employed to find the solution by substituting the optimal PFoPID controller parameters from Table 1 and the related PV system parameters from Table 2 into equation (35), which gives

$$\begin{cases} \left| 1 + \dfrac{j\omega_{b1} + 50}{15(j\omega_{b1})^{1.5} + \frac{120}{(j\omega_{b1})^{1.25}} + 165} \right| = \sqrt{2} \\ \left| 1 + \dfrac{1 - 0.002j\omega_{b2}^2}{0.02(j\omega_{b2})^{1.75} + \frac{0.17}{(j\omega_{b2})^{1.5}} + 0.24} \right| = \sqrt{2} \end{cases} \tag{35}$$

The solution scanning results (with a step size of 10^{-6}) of the closed-loop system by PFoPID controller are provided in Fig. 3, from which one can see that the upper and lower cut-off frequency of q-axis current controller is 0.2954 Hz and 0.6652 Hz, respectively. Thus, its bandwidth is 0.6652 Hz-0.2954 Hz=0.3698 Hz. The upper and lower cut-off frequency of DC-link voltage controller is 1.1392 Hz and 0.5282 Hz, respectively. Hence, its bandwidth is 1.1392 Hz-0.5282 Hz=0.6110 Hz.
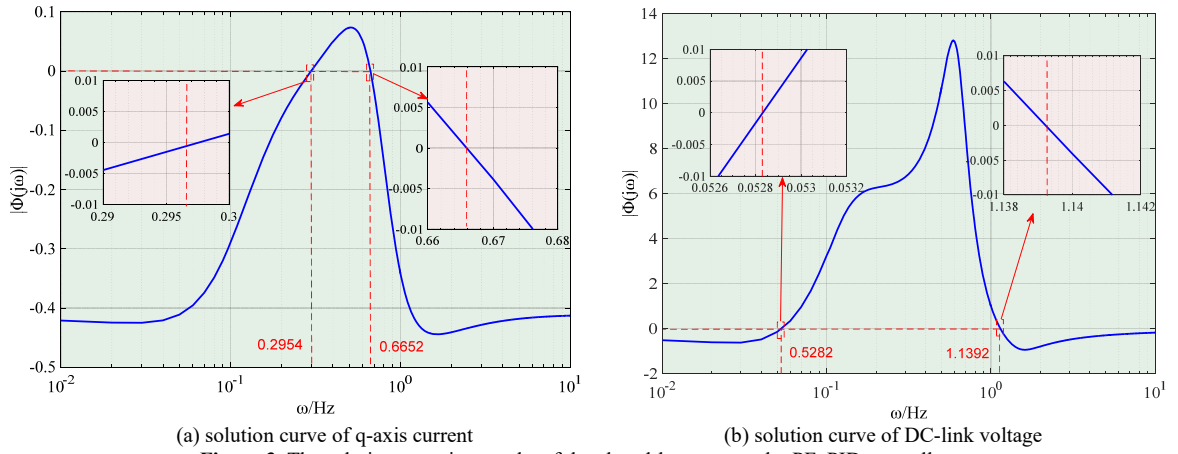
(a) solution curve of q-axis current   (b) solution curve of DC-link voltage

Figure 3. The solution scanning results of the closed-loop system by PFoPID controller.

To this end, the overall control structure of PFoPID control (28) and (29) for PV system (22) to achieve MPPT is shown by Fig. 4, in which the control inputs are modulated by the space vector pulse width modulation (SVPWM) (Bharatiraja et al., 2014).
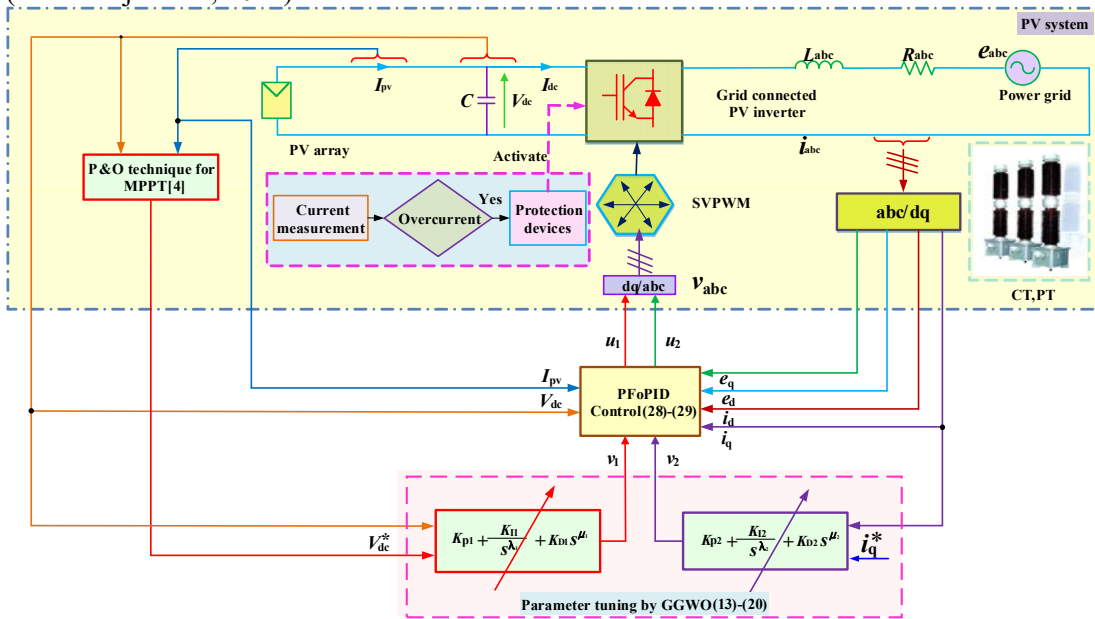
Figure 4. The overall PFoPID control structure of the grid connected PV inverter for MPPT.

5. Case Studies

The proposed PFoPID control is adopted on the grid connected PV inverter to achieve MPPT under different weather conditions. Besides, Table 3 provides the PV system parameters that are taken from Lalili et al., (2011). Here, the initial solar irradiation and temperature are chosen as their rated values, e.g., 1 kW/m^2 and 25℃. Additionally, q-axis current I_q=0. Under such standard operation conditions, the PV output power P=1867 W, DC link voltage V_{dc}=539.5 V, and PV output current I_{pv}=3.46 A, respectively. The simulation is executed on Matlab/Simulink 2016a (MathWorks, Massachusetts, USA) using a personal computer with an IntelR CoreTMi7 CPU at 2.2 GHz and 8 GB of RAM.

Table 3
The PV system parameters.

Typical peak power	60W	**Factor of PV technology (A)**	1.5
Voltage at peak power	17.1V	**Series resistance**	0.21Ω
Current at peak power	3.5A	**Grid voltage (V:rms)**	120V
Short-circuit current (I_{sc})	3.8A	**Grid frequency (f)**	50Hz
Open-circuit voltage (V_{oc})	21.1V	**Grid inductance line (L)**	2mH
Temperature coefficient of I_{sc} (k_1)	3mA/℃	**Grid resistor line (R)**	0.1Ω
Nominal operation cell temperature (T_{ref})	49℃	**DC bus capacitor(C)**	2200μF

5.1 Solar irradiation variation

In order to study the effect of solar irradiation variation on the PV system responses, three consecutive step changes in solar irradiation which decrease from 1 kW/m^2 to 0.5 kW/m^2 at t=0.2 s, increase to 0.8 kW/m^2 at t=0.7 s, and restores to 1 kW/m^2 at t=1.2 s, are carried out, respectively. During the solar irradiation variation, the

temperature maintains at its rated value, e.g., 25℃, for the whole period. Meanwhile, q-axis current I_q is increased to 50 A at t=0.2 s and decreased to -30 A at t=1.2 s. The PV system responses are illustrated in Fig. 5. It shows that PID control presents some DC-link voltage oscillations while FoPID can attenuate such oscillations to some extent. In contrast, PBC and PFoPID control has no oscillation while PFoPID control can track the DC-link voltage and q-axis current at the fastest rate thanks to the energy reshaping and FoPID control mechanism. Moreover, the real-time variation of storage function $H(i_q, V_{dc}, I_{dc})$ illustrates that PFoPID control can simultaneously achieve the fastest tracking rate (steepest slope) and the lowest tracking error (lowest peak value).
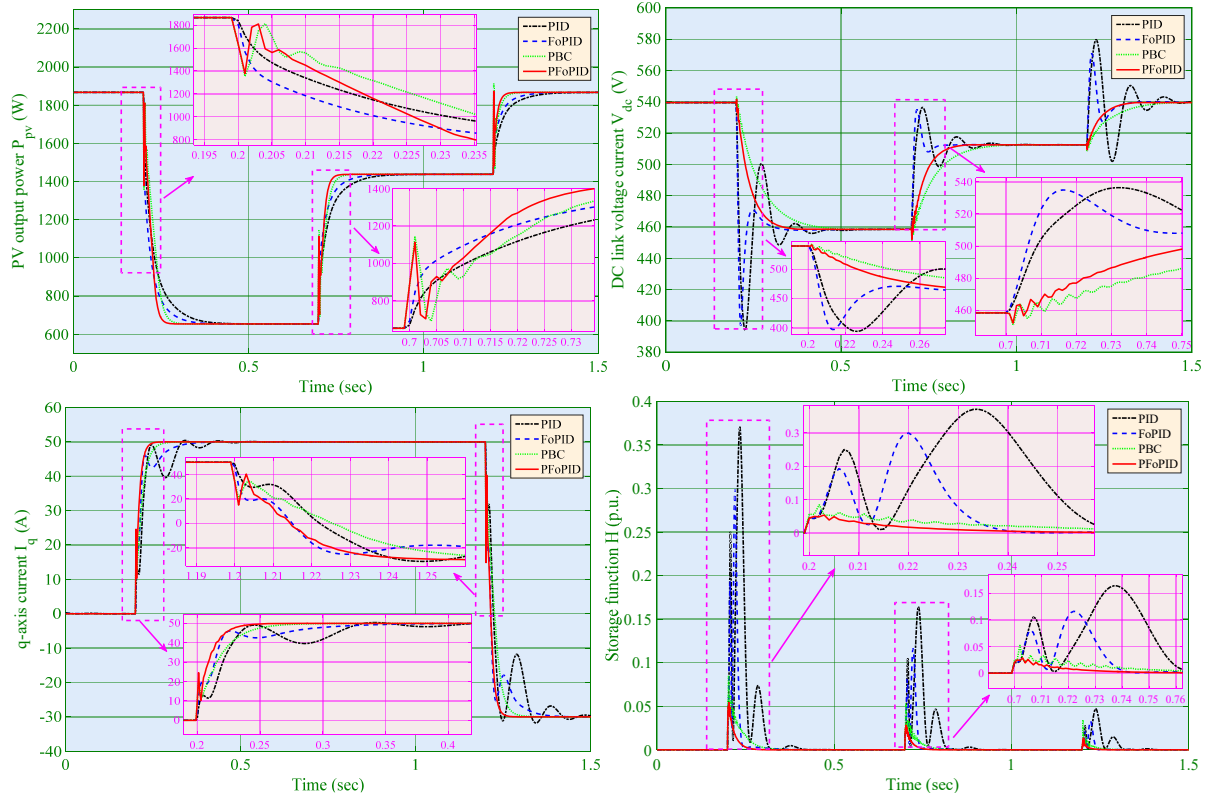
Figure 5. PV system responses obtained under step changes in solar irradiation and q-axis current regulation.

5.2 Temperature variation

In this scenario, two step changes of ambient temperature, e.g., increase from 25℃ to 40℃ at t=0.2 s, and decrease from 40℃ to 25℃ at t=0.95 s, are applied, while the solar irradiation keeps at 1 kW/m². Meanwhile, q-axis current I_q is decreased to -40 A at t=0.2 s and increased to 20 A at t=0.95 s. Figure 10 demonstrates the PV system responses, as shown in Fig. 6, PFoPID can achieve the most satisfactory control performance among four controllers in terms of the fastest tracking rate without any overshoot.
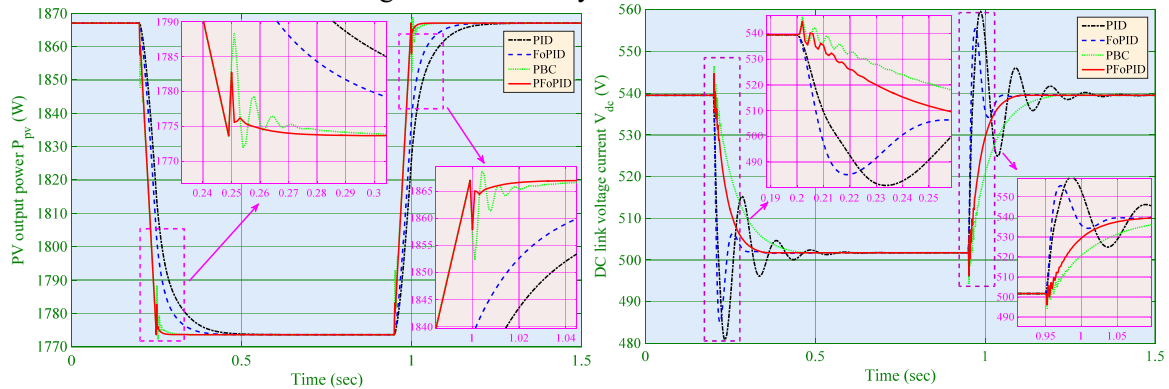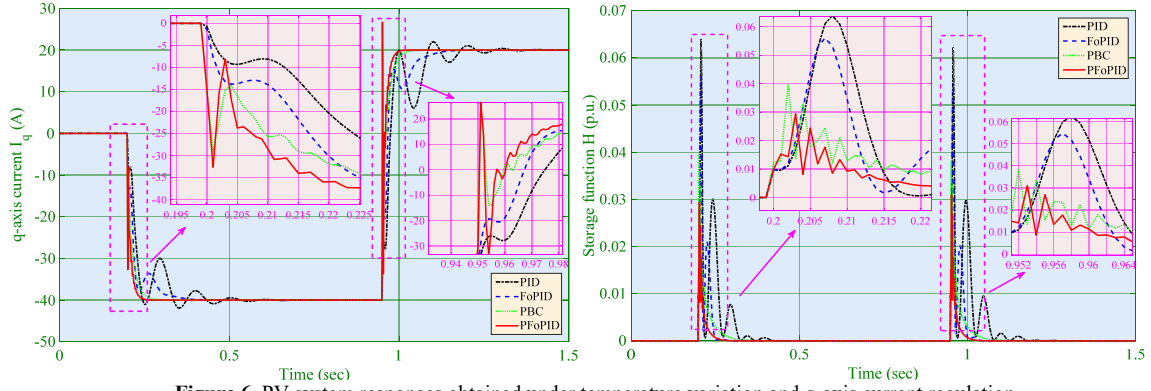
Figure 6. PV system responses obtained under temperature variation and q-axis current regulation.

5.3 Power grid voltage drop

Fault ride-through (FRT) requires the PV system to stay connected and contribute to the power grid in case of severe power grid voltage disturbances as the disconnection may further degrade the voltage restoration during and after the fault (Al-Shetwi et al., 2018; Wang and Ren., 2018). In order to test the FRT capability of the proposed approach, a power grid voltage drop to 0.4 p.u. for 150 ms (t=0.2s-0.35s) (Mojallal and Lotfifard, 2017) at the standard operation condition is undertaken. The PV system responses are given in Fig. 7. One can find that PFoPID control can restore the active power, DC-link voltage, and q-axis current caused by the fault at the fastest rate and lowest oscillations. Hence, it can effectively reduce the malignant effect of the grid fault on the grid connected PV system. Furthermore, the storage function variation shows that a minimal energy oscillation could be achieved by PBC and PFoPID control thanks to the remaining of beneficial terms and nonlinearities compensation, which can actually absorb this amount of destabilizing energy caused by the grid faults.
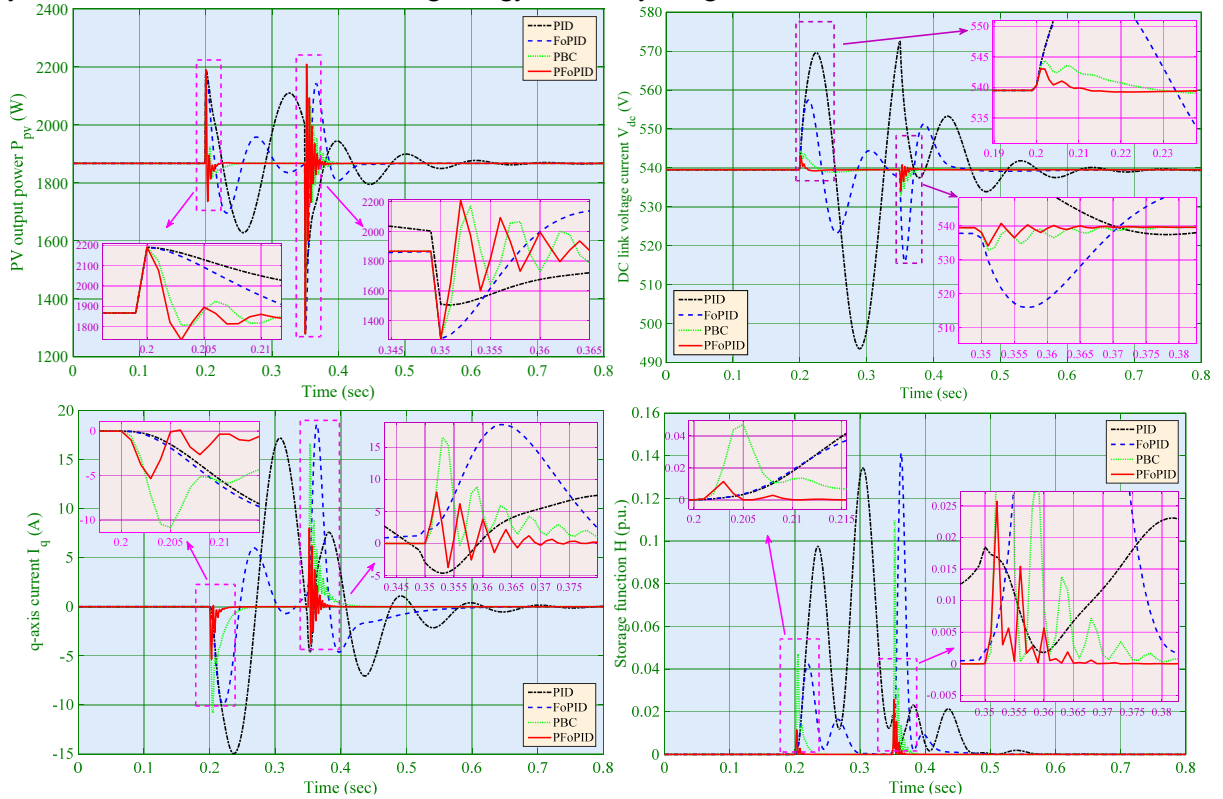

Figure 7. PV system responses obtained under the 60% voltage drop lasting 150 ms at power grid.

5.4 PV inverter parameter uncertainties

In practice, the accurate PV inverter parameters may not be obtained due to the fact of measurement errors, ambient temperature, air density, wear-and-error, etc. As a result, it is important to investigate the robustness of PFoPID control in comparison to other three controllers under PV inverter parameter uncertainties. Here, a series of plant-model mismatches of equivalent resistance R and inductance L associated with ±20% variation around their rated value are studied, in which a 40% voltage drop lasting 100 ms at the power grid is adopted while the absolute peak value of active power $|P|$ is compared. Figure 8 depicts that the variation of absolute peak value of active power $|P|$ obtained by PID control, FoPID control, PBC, and PFoPID control is 10.26%, 9.14%, 6.86%, and 6.43% under resistance uncertainties, respectively. Hence, PFoPID control can provide significant robustness against to PV inverter parameter uncertainties thanks to the retained beneficial terms.

12
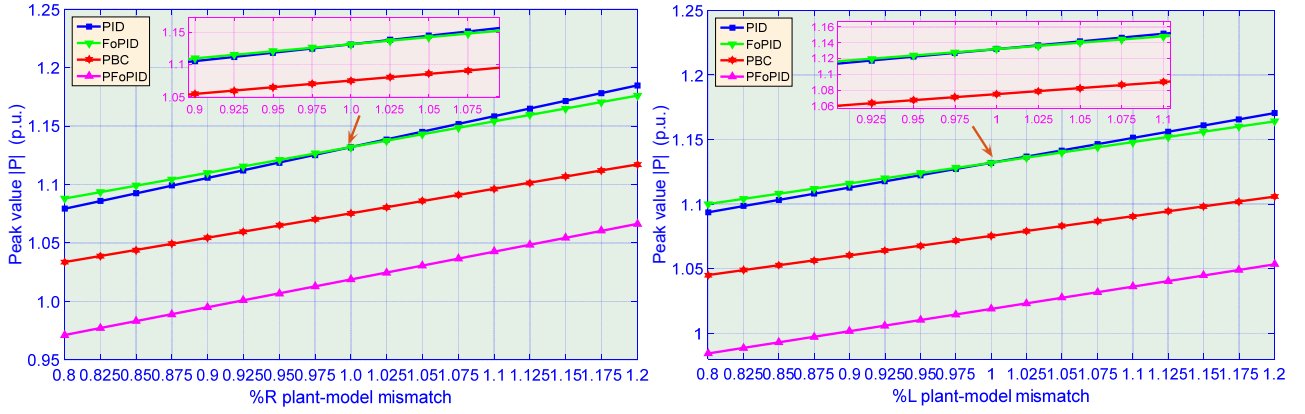
Figure 8. Absolute peak value of active power |P| obtained under a 40% voltage drop lasting 100 ms at power grid associated with ±20% variation of the equivalent resistance R (left panel) and ±20% variation of the equivalent inductance L (right panel) to investigate the PV inverter parameter robustness of four controllers.

5.5 Comparative studies

The integral of absolute error (IAE) indices (Shen et al., 2018, Yao et al., 2015) of four controllers required in the above three cases are tabulated in Table 4 with $IAE_x = \int_0^T |x - x^*|\, dt$. More specifically, $IAE_{Iq} = \int_0^T |I_q - I_q^*|\, dt$ (here x^* means the q-axis current reference I_q^*) and $IAE_{Vdc} = \int_0^T |V_{dc} - V_{dc}^*|\, dt$ (here x^* means the DC-link voltage reference V_{dc}^*). As shown in Table 4, PFoPID control owns the lowest IAE indices, hence it can outperform other three controllers due to the beneficial terms retainment and energy reshaping. In particular, its IAE_{Iq} is merely 74.74%, 77.43%, and 82.31% of that of PID control, FoPID control, and PBC, in the temperature variation, respectively. Meanwhile, its IAE_{Vdc} is just 83.37%, 86.59%, and 91.46% of that of PID control, FoPID control, and PBC, in the power grid voltage drop, respectively.

Table 4
IAE indices (in p.u.) of four controllers obtained in three scenarios.

Scenarios	IAE Indices	PID	FoPID	PBC	PFoPID
Solar irradiation variation	IAE_{Iq}	0.1837	0.1732	0.1611	0.1407
	IAE_{Vdc}	0.4484	0.4412	0.4357	0.3901
Temperature variation	IAE_{Iq}	0.2217	0.2140	0.2013	0.1657
	IAE_{Vdc}	0.5587	0.5431	0.5262	0.4778
Power grid voltage drop	IAE_{Iq}	0.3413	0.3207	0.2938	0.2476
	IAE_{Vdc}	0.7529	0.7249	0.6863	0.6277

Additionally, the summed integral of storage function, e.g., $\int_0^T H(i_q, V_{dc}, I_{dc})\,dt$, obtained under three cases is compared in Fig. 9. It describes the accumulated energy of the PV system resulted from the tracking error, of which a smaller value means a lower overall tracking error. One can find that PID control owns the highest value thus it presents the largest accumulated tracking error among four controllers. In contrast, PFoPID control owns the lowest accumulated tracking error thus it can achieve the most satisfactory control performance.
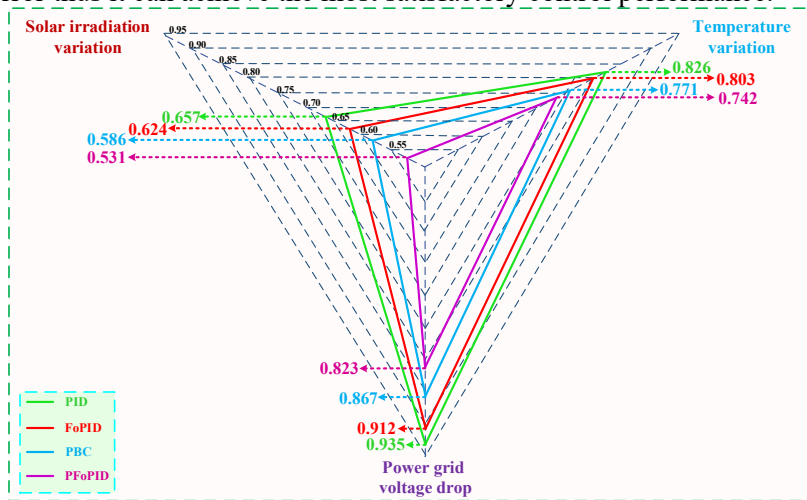
Figure 9. Radar diagram of the overall energy of four controllers obtained in three cases.

Finally, the overall control costs, i.e., $\boldsymbol{u_{costs}} = \int_0^T (|\boldsymbol{u_1}| + |\boldsymbol{u_2}|)\boldsymbol{dt}$, of four controllers required in three cases are compared in Fig. 10. It shows that PFoPID control just requires the lowest overall control costs in all scenarios

13

among four controllers. Particularly, in the power grid voltage drop, its overall control costs are only 92%, 92.6%, and 95.08% to that of PID control, FoPID control, and PBC, respectively.

Lastly, it is worth noting that the improvement of PFoPID control is significant, e.g., the DC-link tracking performance is improved from 9.20% to 14.48%, together with a reduction of control costs from 3.76% to 10.17% in the temperature variation. Hence, PFoPID control ensures the PV systems can always operate economically, stably output power, and optimally extract the solar energy. As the atmospheric conditions vary continously and dramatically in a daliy scale, the overall energy saving (large reduction of control costs in PV inverters) and energy priduction (efficient MPPT and current regulation without overshoot) during whole operation life of PV systems, e.g., normally 15 years, is very prominent.
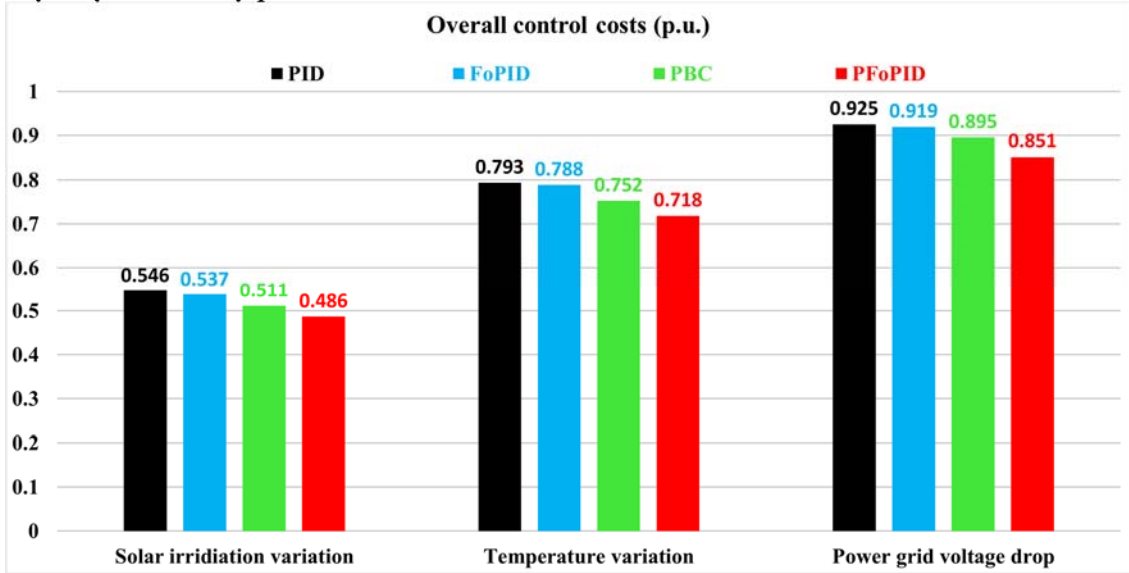

Figure 10. Overall control costs ($\int_0^T (|u_1| + |u_2|)\mathrm{d}t$, with T=3 s) required by four controllers obtained under three cases in p.u. for the control costs comparison.

6. HIL Experiment

HIL experiment offers a reliable and powerful tool for the development and test of complicated real-time embedded systems, which can be employed as an effective platform through adding the complexity of the controlled system into the test platform (Lauss et al., 2016). HIL experiment has been widely employed in PV systems (Khazaei et al., 2015; Bounechba et al., 2016) to validate the implementation feasibility of different types of controllers.

A dSPACE based HIL experiment is undertaken, which configuration and experiment platform are shown by Fig. 11 and Fig. 12, respectively. More specifically, PFoPID based q-axis current and DC-link voltage controller (28)-(29) is implemented on DS1104 board with a sampling frequency f_c=1 kHz. Meanwhile, the PV system is embedded on DS1006 board with a limit sampling frequency f_s= 50 kHz to make HIL simulator as close to the real PV system as possible (Yang et al., 2018a). The measurements of the q-axis current i_q and DC-link voltage V_{dc} are obtained from the real-time simulation of the PV system on the DS1006 board, which are transmitted to PFoPID controller implemented on the DS1104 board for the real-time control inputs calculation.

The main purposes of HIL experiment can be summarized as the following two aspects: 1) Validate the hardware implementation feasibility of the PFoPID controller for PV system; 2) Evaluate the control accuracy and practical computation capability of the PFoPID controller.
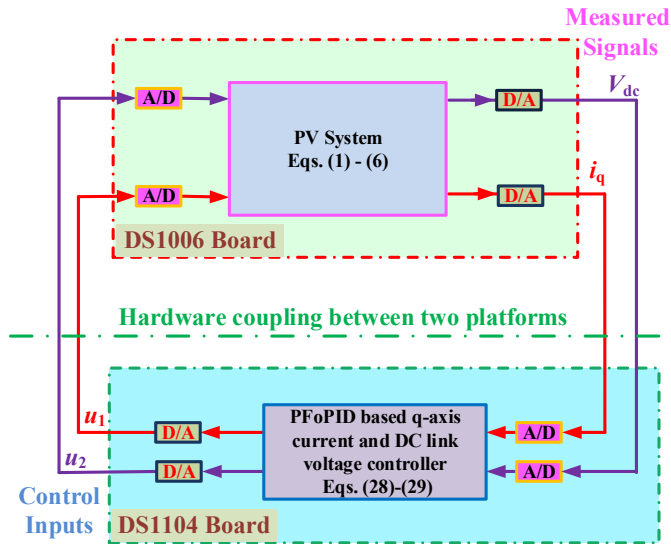
Figure 11. The schematic configuration of HIL experiment.
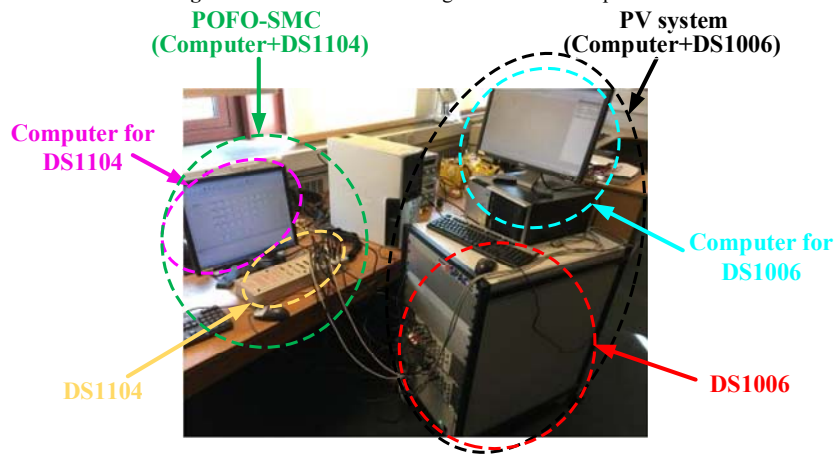

Figure 12. The hardware platform of HIL experiment.

6.1 HIL Experiment: Solar irradiation variation

Figure 13 compares the corresponding PV system responses obtained from the simulation and HIL experiment, which uses the same solar irradiation variation applied in Section 5.1. It can be readily found that the HIL experiment results are very close to the simulation results.
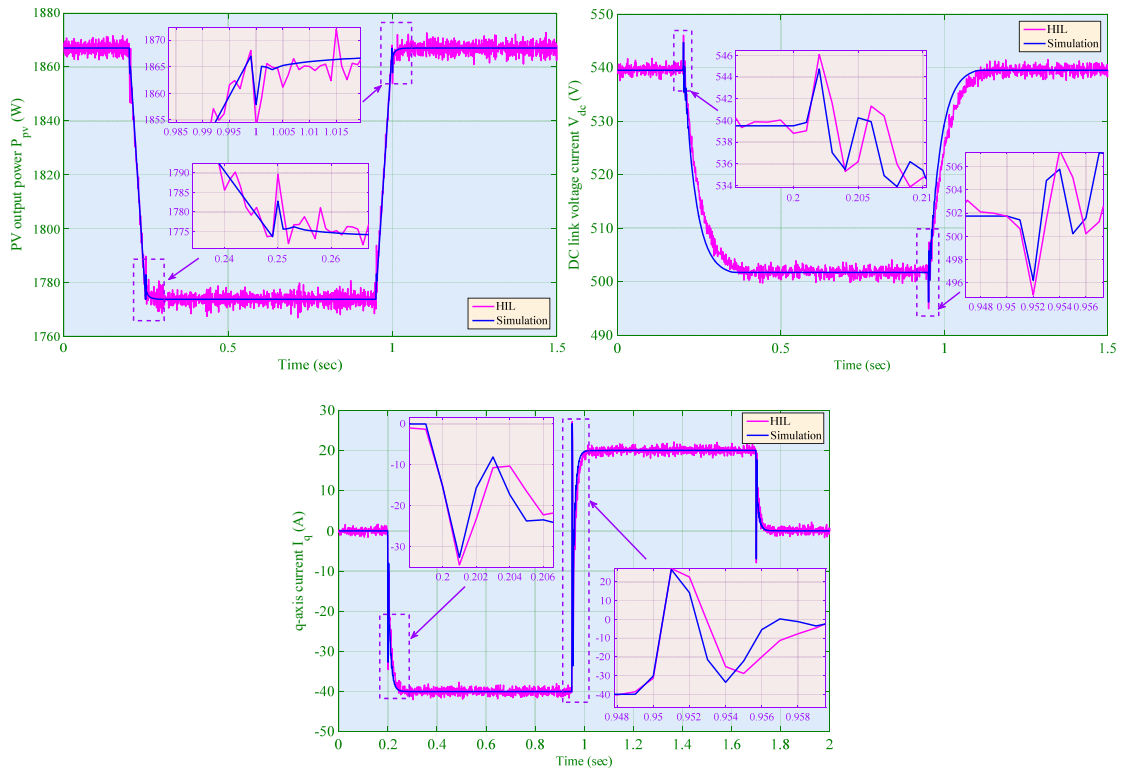

15
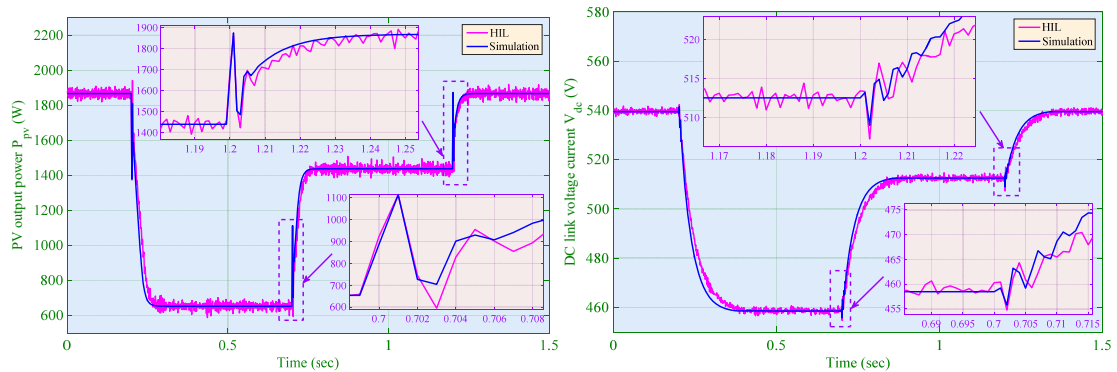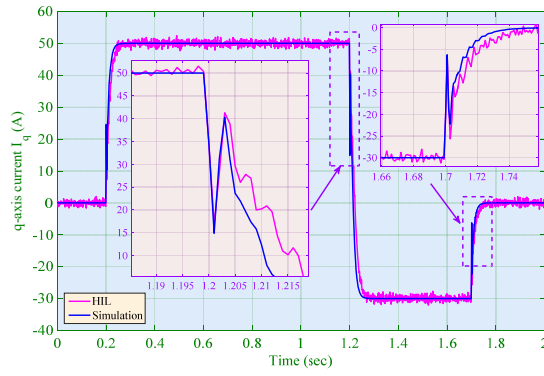
Figure 13. Simulation and HIL experiment results obtained under step changes in solar irradiation and q-axis current regulation.

6.2 HIL Experiment: Temperature variation

The corresponding PV system responses obtained under the same temperature variation used in Section 5.2 are illustrated in Fig. 14, which reveals that the MPPT could be effectively achieved while HIL experiment can provide almost the same control performance to that of simulation.
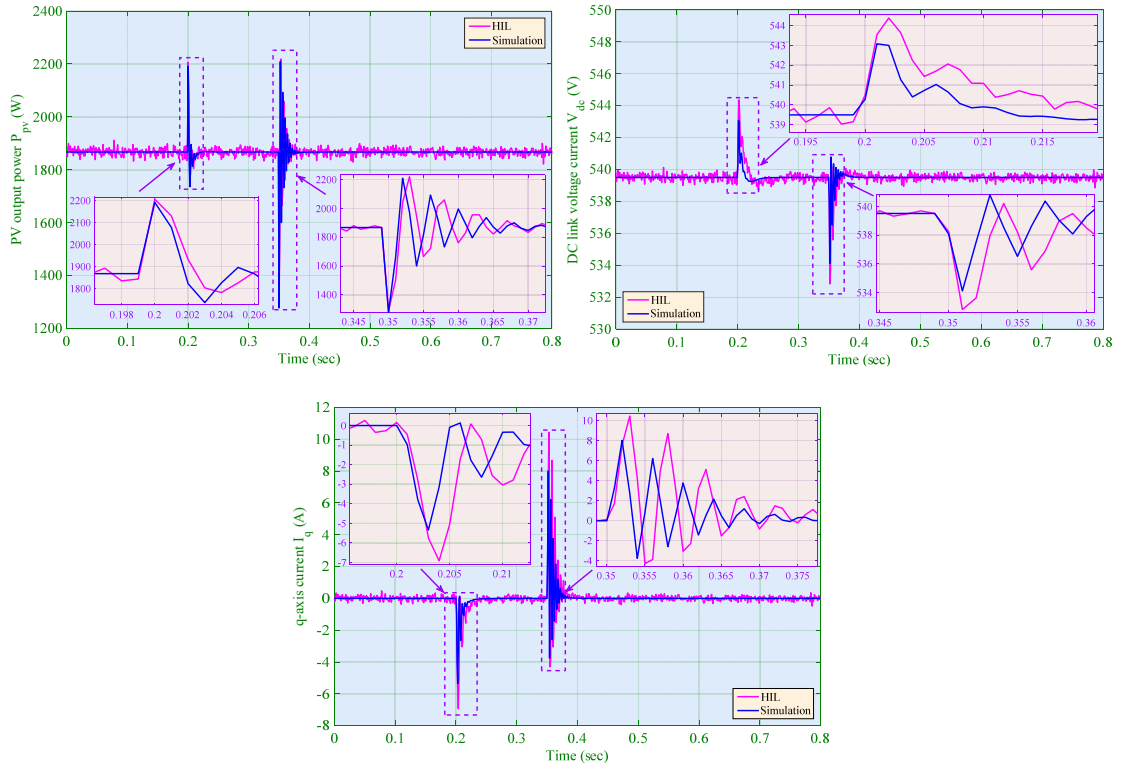

Figure 14. Simulation and HIL experiment results obtained under temperature variation and q-axis current regulation.

6.3 HIL Experiment: Power grid voltage drop

Figure 15 demonstrates the corresponding PV system responses in the presence of the same power grid voltage drop adopted in Section 5.3. One can observe that the HIL experiment results and simulation results are very similar.

Figure 15. Simulation and HIL experiment results obtained under the 60% voltage drop lasting 150 ms at power grid.

To this end, the difference between the simulation results and HIL experiment results is mainly caused by the following three factors:

• The measurement errors and environment noises are ubiquitously existed in the HIL experiment, which leads a consistent oscillation of the HIL experiment results. A filter could be used to suppress the malignant effects of such disturbances to improve the control performance to some extend;

• The sampling frequency of the controller and PV system are the same in the simulation. In contrast, the sampling frequency of the controller is quite smaller than that of the PV system in the HIL experiment to mimic a practical controller;

• The time delay of the controller is evitable in HIL experiment while the simulation does not consider such effect.

7. Conclusions

In this paper, an energy reshaping based PFoPID control is developed and designed for a grid-connected PV inverter to optimally extract solar energy under various operation conditions. The main findings and conclusions are summarized into the following three aspects:

(1) Based on the passivity theory, a storage function associated with DC-link voltage and DC-link current, as well as q-axis current is constructed for the PV system while the physical property of each term is thoroughly investigated and analyzed. Then, the beneficial terms are carefully retained to fully exploit the essential characteristics of the PV system;

(2) FoPID control mechanism is incorporated into the passive control loop as an additional input to reshape the retained energy of the storage function, of which meta-heuristic algorithm called GGWO is employed to optimally tune its control parameters, such that an optimal control performance can be realized;

(3) Simulation results of case studies demonstrate that PFoPID control can achieve the most satisfactory control performance under various atmospheric conditions, together with the lowest overall control costs among all cases. Lastly, a dSpace based HIL experiment is undertaken, which validates the implementation feasibility of the proposed approach.

Acknowledgments

References

Alajmi, B.N.; Ahmed, K.H.; Finney, S.J.; Williams, B.W., 2011, Fuzzy-logic-control approach of a modified hill-climbing method for maximum power point in microgrid standalone photovoltaic system. IEEE Transactions on Power Electronics, 26(4), 1022-1030.

Ahmed, J. and Salam, Z., 2014, A maximum power point tracking (MPPT) for PV system using cuckoo search with partial shading capability. Applied Energy, 119(12), 118-130.

Abdel-Salam, M.; Kamel, R.; Khalaf, M.; Sayed, K., 2015, Analysis of overcurrent numerical-relays for protection of a stand-alone PV system. IEEE Smart Grid Conference, p. 1-6.

Alik, R. and Awang, J., 2017, Modified Perturb and Observe (P&O) with checking algorithm under various solar irradiation. Solar Energy, 148, 128-139.

Al-Shetwi, A.Q.; Sujod, M.Z.; Blaabjerg, F., 2018, Low voltage ride-through capability control for single-stage inverter-based grid-connected photovoltaic power plant, Solar Energy, 159, 665-681

Bao, X.; Wang, J.; Xiang, H.; Ma, Y., 2012, The maximum power point tracking technology of passivity-based photovoltaic grid-connected system. IEEE 7th International Power Electronics and Motion Control Conference-ECCE Asia, Harbin, China, p. 1372-1376.

Bharatiraja, C.; Jeevananthan, S.; Latha, R., 2014, FPGA based practical implementation of NPC-MLI with SVPWM for an autonomous operation PV system with capacitor balancing. International Journal of Electrical Power & Energy Systems, 61, 489-509.

Bounechba, H.; Bouzid, A.; Snani, H.; Lashab, A., 2016, Real time simulation of MPPT algorithms for PV energy system. International Journal of Electrical Power & Energy Systems, 83, 67-78.

Dhar, S. and Dash, P.K., 2016, A new backstepping finite time sliding mode control of grid connected PV system using multivariable dynamic VSC model. International Journal of Electrical Power & Energy Systems, 82, 314-330.

Hilairet, M.; Ghanes, M.; Béthoux, O.; Tanasa, V.; Barbot, J.P.; Normand-Cyrot, D., 2015, A passivity-based controller for coordination of converters in a fuel cell system. IEEE Transactions on Industrial Electronics, 62(8), 5187-5194.

Ishaque, K.; Salam, Z.; Amjad, M.; Mekhilef, S., 2012, An improved particle swarm optimization (PSO)-based MPPT for PV with reduced steady-state oscillation. IEEE Transactions on Power Electronics, 27, 3627-3638.

Kadri, R.; Gaubert, J.P.; Champenois, G., 2011, An improved maximum power point tracking for photovoltaic grid-connected inverter based on voltage-oriented control. IEEE Transactions on Industrial Electronics, 58(1), 66-75.

Kanchanaharuthai, A.; Chankong, V.; Loparo, K.A., 2015, Transient stability and voltage regulation in multimachine power systems vis-à-vis STATCOM and battery energy storage. IEEE Transactions on Power Systems, 30(5), 2404-2416.

Khazaei, J.; Miao, Z.; Piyasinghe, L.; Fan, L., 2015, Real-time digital simulation-based modeling of a single-phase single-stage PV system. Electric Power Systems Research, 123, 85-91.

Kchaou, A.; Naamane, A.; Koubaa, Y.; M'sirdi, N., 2017, Second order sliding mode-based MPPT control for photovoltaic applications. Solar Energy, 155, 758-769.

Kandemir, E.; Cetin, N.S.; Borekci, S., 2017, A comprehensive overview of maximum power extraction methods for PV systems. Renewable and Sustainable Energy Reviews, 78, 93-112.

Kabir, E.; Kumar, P.; Kumar, S.; Adelodun, A.A.; Kim, K.H., 2018, Solar energy: potential and future prospects. Renewable & Sustainable Energy Reviews, 82, 894-900.

Liao, S.W.; Yao, W.; Han, X.N.; Wen, J.Y.; Cheng, S.J., 2017, Chronological operation simulation framework for regional power system under high penetration of renewable energy using meteorological data. Applied Energy, 203, 816-828.

Liu, J.; Wen, J.Y.; Yao, W.; Long, Y., 2016, Solution to short-term frequency response of wind farms by using energy storage systems. IET Renewable Power Generation, 10(5), 669-678.

Lalili, D.; Mellit, A.; Lourci, N.; Medjahed, B.; Berkouk, E.M., 2011, Input output feedback linearization control and variable step size MPPT algorithm of a grid-connected photovoltaic inverter. Renewable Energy, 36, 3282-3291.

Lalili, D.; Mellit, A.; Lourci, N.; Medjahed, B.; Boubakir, C., 2013, State feedback control and variable step size MPPT algorithm of three-level grid-connected photovoltaic inverter. Solar Energy, 98, 561-571.

Loukriz, A.; Haddadi, M.; Messalti, S., 2016, Simulation and experimental design of a new advanced variable step size Incremental Conductance MPPT algorithm for PV systems. ISA Transactions, 62(1), 30-38.

Lauss, G.F.; Faruque, M.O.; Schoder, K.; Dufour, C.; Viehweider, A.; Langston, J., 2016, Characteristics and design of power hardware-in-the-loop simulations for electrical power systems. IEEE Transactions on Industrial Electronics, 63(1), 406-417.

Mirjalili, S.; Mirjalili, S.M.; Andrew, L., 2014, Grey wolf optimizer. Advances in Engineering Software. 69, 46-61.

Messai, A.; Mellit, A.; Guessoum, A.; Kalogirou, S., 2011, Maximum power point tracking using a GA optimized fuzzy logic controller and its FPGA implementation. Solar Energy, 85, 265-277.

Malek, H.; Dadras, S.; Chen, Y.Q., 2014, Application of fractional order current controller in three phase grid-connected PV systems. 2014 American Control Conference (ACC), Portland, Oregon, USA, p. 5224-5229.

Mitkowski, W. and Oprzedkiewicz, K., 2015, Tuning of the half-order robust PID controller dedicated to oriented PV system. Lecture Notes in Electrical Engineering, 320, 145-157.

Mojallizadeh, M.R. and Badamchizadeh, M.A., 2016, Adaptive passivity-based control of a photovoltaic/battery hybrid power source via algebraic parameter identification. IEEE Journal of Photovoltaics, 6(2), 532-539.

Mojallal, A. and Lotfifard, S., 2017, Disturbance estimator-based predictive current controller for single-phase interconnected PV systems. IEEE Transactions on Industry Applications, 53(5), 4201-4209.

Mojallal, A. and Lotfifard, S., 2017, Enhancement of grid connected PV arrays fault ride through and post fault recovery performance. IEEE Transactions on Smart Grid. DOI 10.1109/TSG.2017.2748023.

Naghmasha, Armghan, H.; Ahmad, I.; Armghan, A.; Khan, S.; Arsalan, M., 2018, Backstepping based non-linear control for maximum power point tracking in photovoltaic system. Solar Energy, 159, 134-141.

Ortega, R.; Schaft, A.; Mareels, I.; Maschke, B., 2001, Putting energy back in control. IEEE Control Systems, 21(2), 18-33.

Ortega, R.; Schaf, A.; Castanos, F.; Astolfi, A., 2008, Control by interconnection and standard passivity-based control of port-Hamiltonian systems. IEEE Transactions on Automatic Control, 53(11), 2527-2542.

Oshaba, A.S.; Ali, E.S.; Elazim, S.M.A., 2016, PI controller design using ABC algorithm for MPPT of PV system supplying DC motor pump load. Neural Computing & Applications, 28, 1-12.

Podlubny, I., 1999, Fractional differential equations, Academic Press, New York.

Rezk, H. and Fathy, A., 2107, Simulation of global MPPT based on teaching-learning-based optimization technique for partially shaded PV system. Electrical Engineering, 99(3), 847-859.

Ramadan, H.S., 2017, Optimal fractional order PI control applicability for enhanced dynamic behavior of on-grid solar PV systems. International Journal of Hydrogen Energy, 42(7), 4017-4031.

Shen, Y.; Yao, W.; Wen, J.Y.; He, H.B., 2017, Adaptive wide-area power oscillation damper design for photovoltaic plant considering delay compensation. IET Generation, Transmission and Distribution, 11(18), 4511-4519.

Shen, Y.; Yao, W.; Wen, J.Y.; He, H.B.; Chen, W.B., 2018, Adaptive supplementary damping control of VSC-HVDC for interarea oscillation using GrHDP. IEEE Transactions on Power Systems, **33**(2), 1777-1789.

Song, H.H. and Qu, Y.B., 2013, Energy-based excitation control of doubly-fed induction wind generator for optimum wind energy capture. Wind Energy, 16(5), 645-659.

Tofighi, A. and Kalantar, M., 2011, Power management of PV/battery hybrid power source via passivity-based control. Renewable Energy, 36(9), 2440-2450.

Tang, R. L.; Wu, Z.; Fang, Y.J., 2017, Configuration of marine photovoltaic system and its MPPT using model predictive control. Solar Energy, 158, 995-1005.

Wang, Y. and Ren, B., 2018, Fault ride-through enhancement for grid-tied PV systems with robust control. IEEE Transactions on Industrial Electronics, 65(3), 2302-2312.

Yang, B.; Jiang, L.; Wang, L.; Yao, W.; Wu, Q.H., 2016, Nonlinear maximum power point tracking control and modal analysis of DFIG based wind turbine. International Journal of Electrical Power & Energy Systems, 74, 429-436.

Yang, B.; Zhang, X.S.; Yu, T.; Shu, H.C.; Fang, Z.H., 2017, Grouped grey wolf optimizer for maximum power point tracking of doubly-fed induction generator based wind turbine. Energy Conversion and Management, 133, 427-443.

Yang, B.; Yu, T.; Shu, H.C.; Zhang, Y.M.; Chen, J.; Sang, Y.Y.; Jiang, L., 2018a, Passivity-based sliding-mode control design for optimal power extraction of a PMSG based variable speed wind turbine, Renewable Energy, 119, 577-589.

Yang, B.; Jiang, L.; Yu, T.; Shu, H.C.; Zhang, C.K.; Yao, W.; Wu, Q.H., 2018b, Passive control design for multi-terminal VSC-HVDC systems via energy shaping. International Journal of Electrical Power and Energy Systems, 98, 496-508.

Yang, B.; Yu, T.; Shu, H.C.; Zhang, X.S.; Qu, K.P.; Jiang, L., 2018c, Democratic joint operations algorithm for optimal power extraction of PMSG based wind energy conversion system, Energy Conversion and Management, 159, 312-326.

Yang, B.; Yu, T.; Shu, H.C.; Dong, J.; Jiang, L., 2018d, Robust sliding-mode control of wind energy conversion systems for optimal power extraction via nonlinear perturbation observers. Applied Energy, 210, 711-723.

Yao, W.; Jiang, L.; Wen, J.Y.; Wu, Q.H.; Cheng, S.J., 2015, Wide-area damping controller for power system inter-area oscillations: a networked predictive control approach. IEEE Transactions on Control Systems Technology, 23(1), 27-36.

Zhao, Y.; Lehman, B.; De Palma, J.F.; Mosesian, J., 2011, Challenges to overcurrent protection devices under line-line faults in solar photovoltaic arrays. IEEE Energy Conversion Congress and Exposition, p. 20-27.